34th Symposium on Naval Hydrodynamics
Washington, DC, 26 June -1 July 2022

Assessment of Numerical and Modeling Errors of RANS-based Transition Models for Low-Reynolds Number 2-D Flows

L. Eça[1], R. Lopes[1], S.L. Toxopeus[2], M. Kerkvliet[2], M. Bettle[3],
G. Rubino[4], M. Visonneau[4], B. S. Venkatachari[5], N. Hildebrand[6], M. M. Choudhari[6], C. L. Rumsey[6],
M. Miozzi[7], R. Broglia[7], D. Durante[7], M. Costantini[8] and J.C. Poirier[9]
[1] Instituto Superior Técnico (IST, ULisboa), Portugal,
[2] Maritime Research Institute Netherlands (MARIN), The Netherlands,
[3] Defence Research and Development Canada (DRDC), Canada,
[4] École Centrale de Nantes (ECN), CNRS, France,
[5] National Institute of Aerospace (NIA), USA,
[6] NASA Langley Research Center (NASA-LARC), USA,
[7] National Research Council, Marine Technology Institute (CNR-INM), Italy,
[8] German Aerospace Center (DLR), Germany,
[9] Naval Group, Sirehna, France

Abstract

In this paper we report the outcome of selected workshops organized as part of the NATO Applied Vehicle Technology (AVT)-313 activity *Incompressible Laminar-to-Turbulent Flow Transition Study* that focused on assessing the numerical and modeling accuracy of the γ-Re_θ and γ transition models coupled to the k-ω Shear-Stress Transport (SST) two-equation eddy-viscosity model. Three different test cases involving nominally 2D flow configurations were selected: flow over a flat plate with two different levels of turbulence intensity at the inlet; flow around the Eppler 387 foil at a Reynolds number of 3×10^5 and angles of attack of 1° and 7°; flow around the NACA 0015 foil at a Reynolds number of 1.8×10^5 and angles of attack of 5° and 10°. The flat plate flow conditions correspond to natural and bypass transition, whereas the other two test cases include laminar separation bubbles that lead to separation-induced transition. For each test case, the selected quantities of interest include both integral and local flow quantities.

Geometrically similar grids with a wide range of grid refinement ratios were generated for each of the test cases to allow the estimation of numerical uncertainties for all quantities of interest selected for this study. Several RANS flow solvers were used, employing common grids with the same boundary conditions and mathematical models. Therefore, it is possible to analyze the consistency of the results, i.e., to check if the intervals defined by the different numerical solutions with their respective uncertainties overlap with each other.

Modeling errors can also be addressed for the selected flow quantities that have experimental data available. However, the experimental information available in these cases is not sufficient to guarantee that experiments and simulations are performed with the same settings. Nonetheless, the available experimental data are sufficient to guarantee that modeling errors are significantly reduced with the use of the transition models when compared to simulations performed using only the k-ω SST model.

Introduction

Most traditional naval (and aeronautical) fluid flows occur at large Reynolds numbers ($Re > 10^7$), which often restricts the laminar part of the boundary layer to a very small region near the stagnation point. In these conditions, the accurate prediction of transition from laminar to turbulent flow is irrelevant. On the other hand, model testing leads to flows at Reynolds numbers of the order of 10^6 or even less. However, it is standard practice to force transition to turbulent flow close to the stagnation region to mimic full-scale conditions. Therefore, the well-known early transition predicted by the most popular Reynolds-averaged Navier Stokes (RANS) turbulence models (see for example Eça and Hoekstra [2008]) is actually useful in such cases.

Currently, there is an increased interest in unmanned vehicles with Reynolds numbers in the range of 10^5 to 10^6. In these conditions, the traditional RANS turbulence models become unacceptably inaccurate due to their in-

ability to correctly simulate the transition region. To overcome this shortcoming of RANS, transition models based on transport equations for extra dependent variables have been proposed in the last fifteen years. Two of the most popular models currently available are the γ-Re_θ and γ Local Correlation Transition Models (LCTM) proposed in Menter et al. [2004], Langtry and Menter [2009] and Menter et al. [2015]. These models have been tested in several studies reported in the open literature, for example, Seyfert and Krumbein [2012], Khayatzadeh and Nadarajah [2014], Eça et al. [2016], Baltazar et al. [2018], Kim et al. [2019], Lopes et al. [2020] and Lopes et al. [2022].

In the last three years, several workshops were held as part of the NATO AVT-313 activity *Incompressible Laminar-to-Turbulent Flow Transition Study*. The flow configurations targeted by these workshops included both two-dimensional and three-dimensional test cases. In this paper, we report the outcome of the exercises performed for the two-dimensional test cases that focused mainly on the numerical accuracy of the CFD computations that combine the k-ω Shear-Stress Transport (SST) two-equation eddy-viscosity model, Menter et al. [2003], with the γ-Re_θ and γ LCTM transition models, respectively. Nonetheless, the existence of experimental data for the selected cases also allow a limited assessment of the modeling error. However, the flow conditions (domain sizes and boundary conditions) of experiments and simulations are not always coincident. This means that the estimated modeling errors are not determined by the selected turbulence and transition models alone.

The selected test cases are:

1. Flow over a flat plate with two different levels of turbulence intensity at the inlet, for which experimental skin friction coefficients and mean velocity profiles are available from the Ercoftac Classic Database in Roach and Brierley [1990];

2. Flow around the Eppler 387 foil at a Reynolds number of 3×10^5 and angles of attack of 1° and 7° that have experimentally measured pressure distributions reported in McGhee et al. [1988];

3. Flow around the NACA 0015 foil at a Reynolds number of 1.8×10^5 and angles of attack of 5° and 10°, which have experimentally measured skin friction coefficients reported in Miozzi et al. [2020].

The flat plate flow conditions correspond to natural and bypass transition, whereas the two airfoils include laminar separation bubbles that lead to separation-induced transition. The quantities of interest include integral and local flow quantities, as well as mean flow and turbulence quantities.

For each test case, domain sizes and boundary conditions have been specified to guarantee they are identical for all flow solvers. Sets of geometrically similar grids have been generated (Eça et al. [2002]) covering a wide range of grid refinement ratios. For the flat plate and Eppler 387 airfoil, three different grid topologies have been tested, whereas only one grid topology was proposed for the NACA 0015 airfoil. Simulations were performed with six RANS flow solvers: ANSYS-CFX (DRDC), FUN3D (NASA-LARC), ISIS-CFD (ECN-CNRS), OVERFLOW (NASA-LARC), ReFRESCO (IST/MARIN) and STAR-CCM+ (Sirehna) that include the combinations of the k-ω SST with either γ-Re_θ or γ LCTM transition models. For each flow condition, the quantities of interest have been determined for at least five different refinement ratios and so numerical uncertainties can be estimated for all quantities of interest using the method proposed in Eça and Hoekstra [2014]. The main goal of these solution verification exercises is to check the consistency of the results obtained with the different RANS solvers, i.e., to check if the intervals defined by the different numerical solutions with the respective uncertainties overlap with each other.

The validation exercises (assessment of the modeling error) cannot be performed strictly in compliance with ASME V&V20 Standard, ASME [2009]. Experimental uncertainties are not available for all quantities of interest and not all of the boundary conditions required by the computations are available. Nonetheless, the comparison of the results obtained by combining the k-ω SST model with either γ-Re_θ or γ transition models against the experimental data provides useful information about the modeling performance of the transition models. Furthermore, for the flows around the Eppler 387 and NACA 0015 airfoils, Large-Eddy Simulation (LES) results are also available. LES simulations for the four selected conditions are reported in Catalano and Rosa (2020) and LES results for the NACA 0015 at $\alpha = 5^\circ$ were obtained with Xnavis (CNR-INM). Naturally, the LES simulations did not use the grids proposed for the two-dimensional domains.

A detailed description of all the results collected in this exercise is available at the AVT-313 [2022] website. This paper presents the main trends and conclusions of this study and includes the following sections: mathematical model including a brief description of turbulence and transition models; description of the flow solvers used in this exercise; description of the selected test cases including domain size, boundary conditions, proposed grids and selected quantities of interest; presentation and discussion of the results obtained in the course of solution verification exercises and during comparison with experimental data, and finally, the conclusions.

Mathematical Model

The AVT-313 activity is focused on flows of incompressible fluids that are governed by mass conservation and momentum balance, which can be expressed in a Cartesian coordinate system as

$$\begin{aligned} \frac{\partial \tilde{V}_i}{\partial x_i} &= 0, \\ \frac{\partial \left(\tilde{V}_i\right)}{\partial t} + \frac{\partial \left(\tilde{V}_i \tilde{V}_j\right)}{\partial x_j} &= -\frac{1}{\rho}\frac{\partial \tilde{P}}{\partial x_i} + \frac{1}{\rho}\frac{\partial \tau_{ij}}{\partial x_j} \ , \end{aligned} \tag{1}$$

where $\tilde{V}_i$ are the Cartesian velocity components, ρ is the fluid density, $\tilde{P}$ is the relative pressure[1] and τ_{ij} are the components of the stress tensor, which for a Newtonian fluid are given by:

$$\frac{\tau_{ij}}{\rho} = \nu \left(\frac{\partial \tilde{V}_i}{\partial x_j} + \frac{\partial \tilde{V}_j}{\partial x_i} \right) \ , \tag{2}$$

where ν is the kinematic viscosity of the fluid.

RANS equations

Applying time-averaging to mass conservation, momentum balance and to the flow dependent variables we obtain the Reynolds-averaged continuity and momentum equations,

$$\begin{aligned} \frac{\partial V_i}{\partial x_i} &= 0, \\ \frac{\partial \left(V_i V_j\right)}{\partial x_j} &= -\frac{1}{\rho}\frac{\partial P}{\partial x_i} + \frac{1}{\rho}\frac{\partial \tau_T}{\partial x_j} \ , \\ \frac{\tau_T}{\rho} &= \nu \left(\frac{\partial V_i}{\partial x_j} + \frac{\partial V_j}{\partial x_i} \right) - \overline{v_i v_j} \end{aligned} \tag{3}$$

V_i and P are the mean values of the Cartesian velocity components and pressure, respectively. v_i are the fluctuating part (turbulence) of the Cartesian velocity components and the overbar designates averaging. The Reynolds stress tensor $-\rho\overline{v_i v_j}$ is generated by the two steps of the averaging procedure and requires a turbulence model to close the problem.

In eddy-viscosity models, the so-called Boussinesq approximation determines the Reynolds stress tensor as a function of the mean strain rate and the eddy-viscosity ν_t

$$-\overline{v_i v_j} = \nu_t \left(\frac{\partial V_i}{\partial x_j} + \frac{\partial V_j}{\partial x_i} \right) - \frac{2}{3}\delta_{ij} k, \tag{4}$$

where k is the turbulence kinetic energy and δ_{ij} is the Kronecker symbol. Usually, the contribution of k to the normal stresses is absorbed in the mean pressure gradient term and so the RANS equations (3) become similar to the original equations (1) with three main changes:

- the dependent variables are time-averaged quantities;
- the time derivatives of mean velocity components are zero;
- dynamic viscosity of the fluid is replaced by the effective viscosity $\nu_{\text{eff}} = \nu + \nu_t$.

Turbulence model

In this study, the eddy-viscosity ν_t is determined with the Shear-Stress Transport (SST), two-equation, k-ω turbulence model, Menter et al. [2003]. The transport equations that determine the turbulence kinetic energy k and the specific turbulence dissipation rate ω may be written as

$$V_j \frac{\partial k}{\partial x_j} = P_k - D_k + \frac{\partial}{\partial x_j}\left[\left(\nu + \sigma_k \nu_t\right) \frac{\partial k}{\partial x_j} \right] \ , \tag{5}$$

$$\begin{aligned} V_j \frac{\partial \omega}{\partial x_j} &= \frac{\alpha}{\nu_t} P_k - \beta \omega^2 + \frac{\partial}{\partial x_j}\left[\left(\nu + \sigma_\omega \nu_t\right) \frac{\partial \omega}{\partial x_j} \right] \\ &\quad + 2\left(1 - F_1\right) \frac{\sigma_{\omega 2}}{\omega} \frac{\partial k}{\partial x_k} \frac{\partial \omega}{\partial x_k} \ . \end{aligned} \tag{6}$$

where α, β, σ_k, σ_ω and $\sigma_{\omega 2}$ are constants and F_1 is a blending function. The production term of the k transport equation, P_k, is determined from

$$P_k = \min(\nu_t S^2, 10 D_k) \ . \tag{7}$$

S is the mean strain rate magnitude and D_k is the dissipation term of the k transport equation given by

$$D_k = \beta^* \omega k \ , \tag{8}$$

where β^* is a constant.

The eddy-viscosity is obtained from

$$\nu_t = \frac{a_1 k}{\max\left(a_1 \omega, F_2 S\right)} \ , \tag{9}$$

where a_1 is a constant and F_2 is a function.

As for the transition models described below, constants and functions are not presented here. Their values and definitions are available in the original references.

[1] Reference pressure is the hydrostatic pressure.

Transition models

The $\gamma - Re_\theta$ model, Langtry and Menter [2009], solves two additional transport equations for the intermittency γ and the transition onset momentum thickness Reynolds number $\tilde{R}e_{\theta t}$

$$V_j \frac{\partial \gamma}{\partial x_j} = P_\gamma - E_\gamma + \frac{\partial}{\partial x_j}\left[\left(\nu + \frac{\nu_t}{\sigma_f}\right)\frac{\partial \gamma}{\partial x_j}\right] \quad (10)$$

and

$$V_j \frac{\partial \tilde{R}e_{\theta t}}{\partial x_j} = P_{\theta t} + \frac{\partial}{\partial x_j}\left[\sigma_{\theta t}\left(\nu + \nu_t\right)\frac{\partial \tilde{R}e_{\theta t}}{\partial x_j}\right] \ , \quad (11)$$

where σ_f and $\sigma_{\theta t}$ are constants.

The production term of the γ transport equation P_γ is given by

$$P_\gamma = F_{\text{length}} c_{a1} S \left[\gamma F_{\text{onset}}\right]^{0.5} \left(1 - c_{e1}\gamma\right) \ , \quad (12)$$

where F_{length} is a correlation that controls the length of the transition region, c_{a1} and c_{e1} are constants and F_{onset} is a function that depends on $\tilde{R}e_{\theta t}$.

The low value of γ in the laminar region is maintained by the dissipation term, E_γ, that is written as

$$E_\gamma = c_{a2}\Omega\gamma F_{\text{turb}}\left(c_{e2}\gamma - 1\right) \ , \quad (13)$$

where F_{turb} is a function responsible for deactivating this term in the turbulent region, Ω is the vorticity magnitude and c_{a2} and c_{e2} are constants.

To incorporate the effect of separation-induced transition, the "effective" intermittency γ_{eff} is obtained from

$$\gamma_{\text{eff}} = \max\left(\gamma, \gamma_{\text{sep}}\right) \ , \quad (14)$$

where γ_{sep} is obtained from an additional correlation.

The combination of the $\gamma - Re_\theta$ transition model with the k-ω SST turbulence model is performed by modifying P_k and D_k as:

$$P_k = \gamma_{\text{eff}} P_{k,\text{SST}}, \quad (15)$$

$$D_k = \min\left(\max\left(\gamma_{\text{eff}}, 0.1\right), 1.0\right) D_{k,\text{SST}}, \quad (16)$$

where $P_{k,\text{SST}}$ and $D_{k,\text{SST}}$ are the original production and dissipation terms of the k-ω SST turbulence model. The F_1 blending function definition is modified to $F_1 = \max(F_3, F_{1,\text{SST}})$, where F_3 is a blending function.

The one-equation γ model proposed in Menter et al. [2015] is mainly a simplification of the $\gamma - Re_\theta$ model, that relies only on a single transport equation for the intermittency, which is similar to equation (10), and also guarantees Galilean invariance. However, some of the functions in the production and dissipation terms are changed. In particular, production P_γ is written as

$$P_\gamma = F_{\text{length}} \rho S \gamma F_{\text{onset}}\left(1 - \gamma\right), \quad (17)$$

in which F_{length} is now a constant, whereas for the $\gamma - Re_\theta$ model it was a correlation dependent on the second variable of the model.

The combination of the γ transition model with the k-ω SST turbulence model is done in a similar way to that presented above for the $\gamma - Re_\theta$. However, the details of the modifications of P_k and D_k are not equivalent and are given by:

$$P_k = \gamma P_{k,\text{SST}} + P_k^{\text{lim}} \ , \quad (18)$$

$$D_k = \max\left(\gamma, 0.1\right) D_{k,\text{SST}} \ . \quad (19)$$

The term P_k^{lim} is related to separation-induced transition and is given by

$$\begin{aligned} P_k^{\text{lim}} &= 5\left(1-\gamma\right) F_{\text{on}}^{\text{lim}} S\Omega C_{P_k} \ , \\ C_{P_k} &= \max\left(\gamma - 0.2, 0\right)\max\left(3\nu - \nu_t, 0\right) \ , \end{aligned} \quad (20)$$

where $F_{\text{on}}^{\text{lim}}$ is a function. The blending function F_1 is also modified to $F_1 = \max(F_3, F_{1,\text{SST}})$.

LES equations

Although this exercise is focused on the RANS equations using the k-ω SST turbulence model and the γ-Re_θ and γ transition models, results from Large-Eddy Simulation (LES) approaches are available for two of the selected test cases. The LES equations are also derived from equations (1) applying a filtering process to mass conservation, momentum and flow dependent variables that leads to a set of equations similar to the RANS equations (3). However, there are three main differences:

1. The dependent variables are filtered quantities that depend on space and time;

2. The time derivative of the filtered flow properties is not zero;

3. The unknown residual stress tensor generated by the filtering process can be interpreted as the sum of three tensors and only one of them is similar to the Reynolds stress tensor.

The LES equations require a so-called subgrid scale model to close the system, which in the models used in this exercise also use an eddy-viscosity approach. Although the LES equations become similar to the RANS equations including the time-derivative terms, their solution requires an unsteady three-dimensional approach, whereas the RANS equations are solved for two-dimensional, statistically steady flows.

Flow Solvers

Unless stated, all flow solvers were applied for the solution of the time-averaged RANS equations with the k-ω SST two-equation turbulence model, Menter et al. [2003], in conjunction with the γ-Re_θ, Langtry and Menter [2009], or γ, Menter et al. [2015] , transition models using a steady-state approach.

ANSYS-CFX

ANSYS-CFX is a general purpose CFD software suite that has compressible and incompressible solvers and a wide variety of turbulence models. ANSYS-CFX uses an element-based finite volume method to discretize the equations. All solution variables are collocated at mesh vertices (nodes) and Rhie-Chow interpolation is used for pressure-velocity coupling. Second-order accurate trilinear shape functions were used to evaluate the diffusion terms and pressure gradients. ANSYS-CFX's high-resolution discretization scheme was used for the advection terms in all equations. This is an upwind-biased discretization scheme that is nominally second-order accurate. However, it uses a blending function, which can locally reduce the order of accuracy to as low as 1 in regions of sharp gradients to achieve a bounded solution. ANSYS-CFX uses a coupled solver and an algebraic multi-grid procedure (Raw [1996]) to accelerate the solution.

FUN3D

The suite of codes known as FUN3D is an unstructured node-centered upwind-biased implicit RANS flow solver, Anderson and Bonhaus [1994]. FUN3D uses a finite-volume method. The inviscid fluxes are calculated with a Roe-Riemann solver, Roe [1981]. For second-order accuracy, the interface values are obtained by extrapolation of the centroidal values of the control volumes (based on gradients computed at the mesh vertices with an unweighted least-squares technique). The viscous fluxes are discretized such that velocity gradients on dual faces are calculated with the Green-Gauss theorem. Pseudotime integration is performed with a backward Euler scheme. The linear system of equations at each time step is numerically solved with a point implicit procedure or an implicit line relaxation scheme, Nielsen et al. [2004]. Biedron and et al. [2020] is the most recent version of the FUN3D manual.

ISIS-CFD

The solver ISIS-CFD, available as a part of the FINE™/Marine computing suite distributed by Cadence Design Systems, is an incompressible multiphase unsteady Reynolds-averaged Navier-Stokes (URANS) solver mainly devoted to marine hydrodynamics. It is based on a fully-unstructured (face-based) finite volume discretization with specific functionalities needed for multiphase flows and industrial applications (see Leroyer and Visonneau [2005], Queutey and Visonneau [2007], Wackers et al. [2013]). ISIS-CFD uses a fully-collocated arrangement with the dependent variables stored at the cell centers. Second-order discretization schemes have been applied to all transport equations including turbulence and transition quantities. The constant in the production term of the k transport equation detailed in Eq. 7 was changed from 10 to 15 for the flat plate simulations, whereas the airfoils calculations were performed with equation (Eq. 7) replaced by the Kato and Launder [1993] approach.

OVERFLOW

The NASA OVERFLOW 2.3b, Nichols and Buning [2019], is an implicit structured overset grid Navier-Stokes solver that is capable of computing time-accurate and steady-state solutions via a variety of options for spatial and temporal discretization. All the solutions reported in this work were obtained by running the OVERFLOW solver in a steady-state manner by using the third-order Roe upwind scheme, Roe [1981], and the unfactored successive symmetric overrelaxation (SSOR) implicit solution algorithm, Nichols et al. [2006]. third-order discretization was utilized for the convective terms in all the transport equations, while the gradients were evaluated using second-order accurate discretization.

ReFRESCO

ReFRESCO is a CFD solver based on a finite volume discretization of the continuity and momentum equations written in strong conservation form. The solver uses a fully-collocated arrangement and a face-based approach that enables the use of cells with an arbitrary number of faces. Picard linearization and mass conservation is ensured using a SIMPLE-like algorithm, Klaij and Vuik [2013], and a pressure-weighted interpolation technique to avoid spurious oscillations, Miller and Schmidt [1988]. Thorough code verification is performed for all releases of ReFRESCO, Eça et al. [2016]. Simulations were performed with a segregated approach using second-order

schemes for the discretization of all terms of the transport equations, with the exception of the convective terms that include flux limiters. Furthermore, first-order schemes are applied to the k and ω transport equations to enhance iterative convergence. For one of the test cases, second-order schemes with limiters were also used for the convective terms of the k and ω transport equations. For all simulations reported in this paper, the constant of the production limiter of the k transport equation (Eq. 7) was changed to 15.

STAR-CCM+

STAR CCM+ v2021.3 is a commercial CFD package based on a finite volume discretization and Picard linearization. Selected space discretization schemes were all second-order accurate and no production limiter (equation 7) was used in the k-ω SST turbulence model. Furthermore, the implementation of the γ-Re_θ model, as detailed in Langtry and Menter [2009], within the the solver was done by researchers at Sirehna.

χnavis

LES simulations were performed for the NACA 0015 test case at $\alpha = 5^\circ$ using χnavis, which is a general purpose unsteady RANS solver, developed at the Institute of Marine Engineering (INM-CNR) of Italy (Di Mascio et al. [2007], Di Mascio et al. [2009] and Broglia and Durante [2018]). The code is based on a finite volume discretization of the governing equations that uses second order accurate schemes in space and in time. Complex geometries and bodies in relative motion are handled by an in-house developed dynamical overlapping grid approach. For the LES simulations reported here, the WALE model of Franck and Ducros [1999] has been used. This subgrid scale model has been proven to be reliable for cases where both turbulent and laminar flow regimes are present, and it is also able to reproduce the correct behaviour of the velocity fluctuations toward the wall without any additional damping function.

LASSIE

The LES results reported in Catalano and de Rosa [2020] were obtained with the LASSIE code that was originally inherited from CIRA in the framework of the affiliation program to CTR (Center for Turbulence Research), Stanford University /NASA Ames, Wang et al. [2001] and Catalano et al. [2003]. The code employs an energy-conservative numerical scheme. Second-order central differences in streamwise and wall-normal directions, and Fourier collocations in the spanwise direction are used. The code is written in body-fitted coordinates with a staggered arrangement of the flow variables. The fractional step approach in combination with the Crank-Nicholson method for the viscous terms and the third-order Runge-Kutta scheme is used for the time advancement. The continuity constraint is imposed at each Runge-Kutta substep by solving a Poisson equation for the pressure. The subgrid scale stress tensor is modeled by the dynamic Smagorinsky model in combination with a least-square contraction and spanwise averaging.

Test Cases

Flow over a flat plate

Transitional flows over a flat plate are Case 20 of the ERCOFTAC (European research community on flow, turbulence and combustion) Classic Database for which there are experimental measurements of skin friction coefficient C_f and mean horizontal velocity V_x profiles available in Roach and Brierley [1990]. Unfortunately, no measurement uncertainty is reported. Nonetheless, it is indicated that different techniques were used to determine C_f within a variability of 2%, which we have assumed as the bound on the experimental uncertainty in both C_f and V_x. The experimental apparatus uses a 0.02mm thick plate with a sharp bevelled leading edge over the first 0.2m. From the several flow conditions available in the ERCOFTAC Classic Database, two cases were selected: T3AM (or T3A-) that corresponds to natural transition and T3A that exhibits bypass transition.

The selected computational domain is a rectangle of length $1.5L$ ($-0.25L \leq x \leq 1.25L$) and height of $0.25L$ ($0 \leq y \leq 0.25L$), where L is the length of the plate. The leading edge of the plate is at the origin of the coordinate system and the x axis is aligned with the plate. The Reynolds number, based on the velocity of the incoming flow V_∞, L and ν is $Re = 10^7$.

For the two flow setting (T3AM and T3A), proposed boundary conditions are identical at four of the five boundaries. Constant pressure is imposed at the top boundary ($y = 0.25L$) and normal derivatives of all remaining dependent variables are set equal to zero. At the outlet of the domain ($x = 1.25L$), zero streamwise derivatives are applied to all dependent variables. Symmetry conditions are applied upstream and downstream of the plate on the bottom boundary ($y = 0$). At the plate surface, impermeability and no-slip conditions lead to zero velocity components, $V_x = 0$ and $V_y = 0$. The shear-stress at the wall is calculated directly from its definition

(no wall functions) and the pressure derivative in the normal direction is set equal to $\partial P/\partial y = 0$. The turbulence kinetic energy is set equal to $k = 0$ and the specific turbulence dissipation rate ω is obtained from the near-wall analytic solution[2], Wilcox [1998]. Normal derivatives of the dependent variables of the transition models are set equal to zero.

Table 1 summarizes the boundary conditions proposed for the inlet boundary. Experimental information is only available for the horizontal velocity component V_x and for the turbulence intensity I. The values of the inlet eddy-viscosity ν_t were tuned with the combination k-ω SST plus γ-Re_θ to match the experimental C_f distribution.This choice is motivated by the location of the inlet boundary $0.25L$ upstream of the leading edgge, which does not allow to match I at the leading edge and its decay rate with the values measured in the experiment. k and ω are a consequence of the selected values for I and ν_t and $\tilde{R}e_{\theta t}$ can be calculated from the values of the other dependent variables.

Table 1: Proposed inlet boundary conditions for the simulation of the flow over a flat plate.

Variable	T3AM	T3A
V_x	V_∞	V_∞
V_y	0	0
P	$\partial P/\partial x = 0$	$\partial P/\partial x = 0$
k	$1.504 \times 10^{-4} V_\infty^2$	$4.319 \times 10^{-3} V_\infty^2$
ω	$60.1621 V_\infty/L$	$154.25 V_\infty/L$
γ	1	1
I	0.0100135	0.0536609
ν_t	25ν	280ν

Grid sets

Three different sets of geometrically similar grids have been generated for the calculation of the flow over a flat plate: a set of 5 Cartesian grids (H topology); a set of 5 multiblock grids with O-topology at the leading and trailing edges of the plate; a set of 9 multiblock grids with HO topology at the leading and trailing edges of the plate. Naturally, the simplest grids are those with the H topology. However, the use of high aspect ratio cells in the wake of the plate can cause iterative convergence problems to the flow solvers. Therefore, the O and HO sets preserve the same grid line spacing in the near-wall region but avoid the high aspect ratio cells upstream and downstream of the plate.

[2]Some flow solvers impose the ω value at the near-wall cell center, whereas others determine ω at the same location and impose a value 10 times larger at the boundary face Menter et al. [2003].

For all these grid sets, the grid refinement ratio $r_i = h_i/h_1$ can be computed from the number of faces on the plate surface N_{plate}, where the typical cell size $h_i \propto 1/N_{\text{plate}}$ and so $r_i = h_i/h_1 = (N_{\text{plate}})_1/(N_{\text{plate}})_i$. Table 2 presents N_{plate} and r_i for the grids of the three sets. h_1 is obtained from the finest grid of the HO set. The number of grid cells for the finest grids of each set are approximately 0.29×10^6 for the H set, 0.17×10^6 for set O and 2×10^6 for set HO. Nondimensional heights of the near-wall cells in wall coordinates are below $y^+ = 1$ for all grids and the stretching functions proposed by Vinokur [1983] defined the increase of the cells height in the near-wall region. Maximum values of y^+ are close to 0.8 for the largest value of r_i and approximately equal to 0.2 for the finest HO grid. Figure 1 illustrates the O and HO topology grids at the leading edge (the H set includes Cartesian grids). All flat plate grids are symmetric with respect to $x = 0.5L$ and so the same topology is used at the trailing edge.

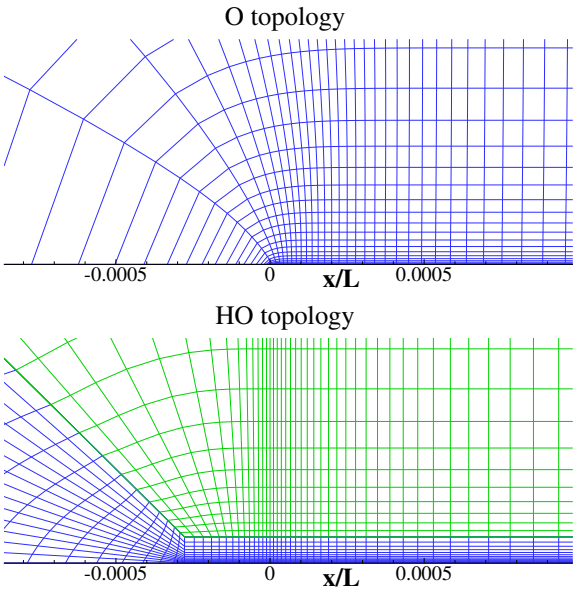

Figure 1: Illustration of the O and HO topology grids at the leading edge of the flat plate.

Quantities of interest

The selected quantities of interest are the skin friction, C_f, distribution on the surface of the plate and V_x, k, ν_t and γ profiles at three locations: one in the laminar flow region ($x = 0.10381L$ for T3AM and $x = 0.01006L$ for T3A), one in the transition region ($x = 0.18281L$ for T3AM and $x = 0.02035L$ for T3A) and one in the turbulent flow region ($x = 0.20216L$ for T3AM and $x = 0.05273L$ for T3A). Experimental data are available

Table 2: Number of faces on the plate surface N_{plate} and grid refinement ratio $r_i = h_i/h_1$ for the three grid sets proposed for the calculation of the flow over a flat plate.

Grid	H topology		O topology		HO topology	
	N_{plate}	r_i	N_{plate}	r_i	N_{plate}	r_i
1	1024	2.5	1024	2.5	2560	1.
2	896	2.86	896	2.86	2048	1.25
3	768	3.33	768	3.33	1792	1.43
4	640	4.	640	4.	1600	1.6
5	512	5.	512	5.	1280	2.
6					1024	2.5
7					896	2.85
8					768	3.2
9					640	4.

for C_f and for the V_x profiles, Roach and Brierley [1990].

Flow around the Eppler 387 airfoil

The flow around the Eppler 387 airfoil at low Reynolds numbers has been experimentally addressed in McGhee et al. [1988], Cole and Mueller [1990] and Selig [1995]. In the present exercise, we have selected a Reynolds number based on the velocity of the incoming flow V_∞, airfoil chord c and ν of $Re = 3 \times 10^5$ and the angles of attack of $\alpha = 1^\circ$ and $\alpha = 7^\circ$. Pressure distributions are reported in McGhee et al. [1988] for these flow settings and a Mach number of 0.09. The height of the test section and the wind-tunnel length are equal to $15c$ and the span of the test wing is $6c$. No blockage corrections have been applied to the pressure coefficients. From the information reported in McGhee et al. [1988], we have assumed that the experimental uncertainty of the pressure coefficient C_p measurements is 0.25%.

The domain for the calculation of the flow around the Eppler 387 airfoil is a rectangle of length $36c$ and width $24c$. The leading edge of the airfoil is at the origin of the coordinate system $(x = 0, y = 0)$ and the x axis is aligned with the incoming flow. The inlet is located $12c$ upstream of the leading edge of the airfoil ($x = -12c$) and the outlet is placed $24c$ downstream of the leading edge of the airfoil ($x = 24c$). The outer boundary is located $\pm 12c$ away from the horizontal line that contains the leading edge of the airfoil ($y = 0$). Figure 2 illustrates the domain for the calculation of the flow around the Eppler 387 airfoil.

Selected boundary conditions are: pressure imposed at the outlet boundary and derivatives with respect to x equal to zero for all other dependent variables; free slip conditions at the top and bottom boundaries, which means that $V_y = 0$ and derivatives with respect to y of all remaining variables are equal to zero; at the airfoil surface mean velocity components and turbulence kinetic energy are equal to zero, normal derivatives of pressure and dependent variables of the transition models are set equal to zero and ω is obtained from the near-wall analytic solution. At the inlet boundary, all dependent variables are specified with the exception of the pressure that is extrapolated from the interior of the domain. The proposed values are $V_x = V_\infty$, $V_y = 0$, $k = 1.5 \times 10^{-4} V_\infty^2$, $\omega = 1.5 \times 10^4 V_\infty / L$ and $\gamma = 1$. The values of k and ω are obtained from a turbulence intensity $I = 0.01$ and $\nu_t = 3 \times 10^{-3} \nu$.

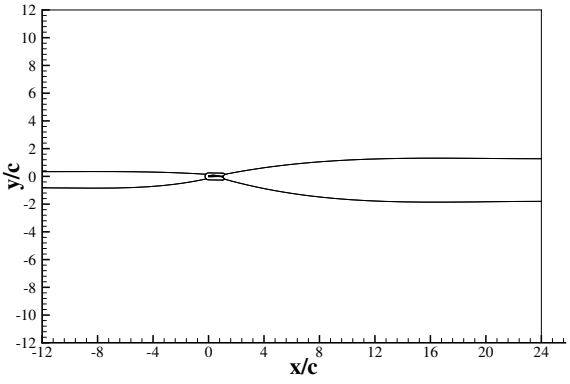

Figure 2: Illustration of the domain for the calculation of the flow around the Eppler 387 airfoil.

Grid sets

Three sets of multiblock geometrically similar grids were generated for the domain depicted in Figure 2. The three sets have different topologies in the vicinity of the airfoil embedded in an H topology that fits the rectangular domain. The C set has 5 grids with a C topology around the airfoil and so the high-aspect ratio of the near-wall cells is also used in the wake of the airfoil; 5 O topology grids are included in the O set and a combination of C and O topologies is adopted for 9 grids of the CO set. The near-wall cell heights of the coarsest grids of the three sets are similar and lead to a maximum value of y^+ close to 0.5. On the other hand, the longitudinal grid line spacing at the trailing edge is significantly different in the three sets. As for the flat plate grids, stretching functions proposed by Vinokur [1983] are used to define the changes in the grid line spacing at the block boundaries. Figure 3 illustrates the grids in the airfoil vicinity and at the trailing edge of the airfoil for $\alpha = 1^\circ$ and $\alpha = 7^\circ$ with $Re = 3 \times 10^5$.

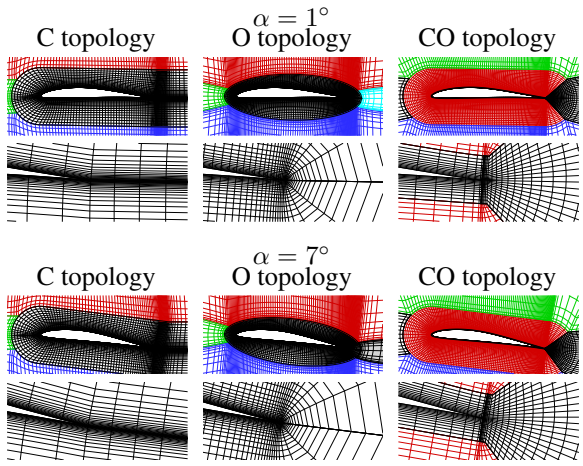

Figure 3: Illustration of the C, O and CO topology grids for the calculation of the flow around the Eppler 387 airfoil at $\alpha = 1^\circ$ and $\alpha = 7^\circ$ with $Re = 3 \times 10^5$.

The grid refinement ratio is defined by $r_i = h_i/h_1 = (N_{\text{foil}})_1/(N_{\text{foil}})_i$ with h_1 corresponding to the typical cell size of the finest grid of set CO. Table 3 presents N_{foil} and r_i for the three grid sets. The finest grids of each set include approximately 0.93×10^6 cells for the C set, 0.26×10^6 cells for the O set and 3.5×10^6 for the CO set.

The LES simulations reported in Catalano and de Rosa [2020] were performed with a C-topology grid contatining 1328×196 cells in the $x - y$ plane and 96 cells in the z spanwise direction, which is approximately 25×10^6 cells with 0.26×10^6 cells in the $x - y$ plane.

Table 3: Number of faces on the airfoil surface N_{foil} and grid refinement ratio $r_i = h_i/h_1$ for the three grid sets proposed for the calculation of the flow around the Eppler 387 airfoil.

Grid	C topology		O topology		CO topology	
	N_{foil}	r_i	N_{foil}	r_i	N_{foil}	r_i
1	960	3.2	960	3.2	3072	1.
2	840	3.66	840	3.66	2560	1.2
3	720	4.27	720	4.27	2048	1.5
4	600	5.12	600	5.12	1792	1.71
5	480	6.4	480	6.4	1536	2.
6					1280	2.4
7					1024	3.
8					896	3.42
9					768	4.

Quantities of interest

The selected quantities of interest include integral and local flow quantities. Integral quantities are the coefficients of lift, C_L, and drag C_D as well as the friction and pressure components of C_D. Pressure coefficient, C_p, and skin friction coefficient, C_f, on the airfoil surface are the local flow quantities. Experimental data are available for C_p, McGhee et al. [1988].

Flow around the NACA 0015 airfoil

The experiments of the flow around the NACA 0015 were conducted in the CEIMM cavitation tunnel (CNR-INM, Rome, IT), a closed-loop water facility with a nozzle contraction ratio of 5.96:1 and a square test section, having side $B = 600$mm, length $L = 2.6$m and optical access. Within the test section, freestream turbulence is less than 2%, while the flow uniformity is less than 3% for the vertical component and 1% for the axial one. The aluminum hydrofoil has the symmetric shape of an NACA 0015 profile, a chord length $c = 120$mm, and a span width equal to the test-section side ($B = 600$mm), which correspond to an aspect ratio and blockage factor of $B/c = 5$ and $c/B = 0.2$, respectively. The model is mounted vertically in the middle of the tunnel transverse side and rotated around its geometric center to set the profile at the investigated angles of attack $\alpha = 5^\circ$ and $\alpha = 10^\circ$ Miozzi et al. [2019]. The Reynolds number, based on V_∞ and c is equal to $Re = 1.8 \times 10^5$. Experimental measurements of the skin friction C_f coefficient are performed using a Temperature Sensitive Paint (TSP). Details of the measuring technique are reported in Miozzi et al. [2020].

The domain for the calculation of the flow around the NACA 0015 airfoil at angles of attack of $\alpha = 5^\circ$ and $\alpha = 10^\circ$ is a rectangle that matches the dimensions of the experimental facility: length $21.7c$ and width $5c$. The center of the airfoil (half-chord) is at the origin of the coordinate system $(x = 0, y = 0)$ and the x axis is aligned with the incoming flow. The inlet is located $7.2c$ upstream of the center of the airfoil ($x = -7.2c$) and the outlet is placed $14.5c$ downstream of the center of the airfoil ($x = 14.5c$). The outer boundary is located $\pm 2.5c$ away from the horizontal line that contains the center of the airfoil ($y = 0$). The domain is illustrated in figure 4.

Boundary conditions are the same as those described above for the Eppler 387 airfoil. However, suggested values of turbulence intensity and inlet eddy-viscosity are $I = 0.005$ and $\nu_t = 1.8 \times 10^{-3}\nu$ that lead to $k = 3.75 \times 10^{-5} V_\infty^2$ and $\omega = 3.75 \times 10^3 V_\infty / L$.

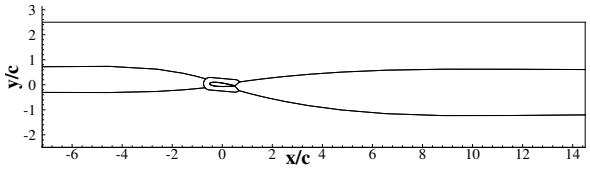

Figure 4: Illustration of the domain for the calculation of the flow around the NACA 0015 airfoil.

Grid sets

For the NACA 0015 airfoil at $\alpha = 5°$ and $\alpha = 10°$ only the 9 grids of the CO set were generated using the same grid densities as for the Eppler 387 airfoil. Therefore, the numbers included in Table 3 also apply to the NACA 0015 grids. Near-wall cell height ensures a maximum y^+ close to 0.5 for the coarsest grid of the set. Figure 5 illustrates the grids generated for the calculation of the flow around the NACA 0015 airfoil at $\alpha = 5°$ and $\alpha = 10°$ for $Re = 1.8 \times 10^5$.

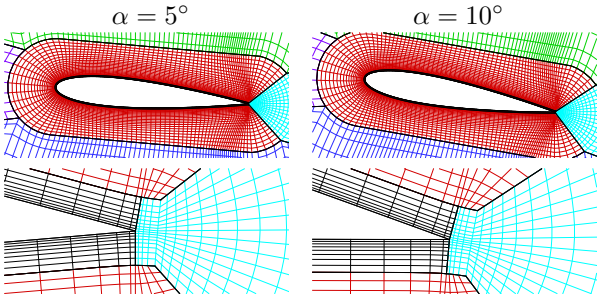

Figure 5: Illustration of the CO topology grids for the calculation of the flow around the NACA 0015 airfoil at $\alpha = 5°$ and $\alpha = 10°$ and $Re = 1.8 \times 10^5$.

LES simulations reported in Catalano and de Rosa [2020] were performed in C grids with the number of cells equal to that presented above for the Eppler 387 airfoils. The LES simulations performed with χnavis were carried out using an O-type multiblok grid with a total of 71×10^6 cells. The outer (cylindrical) boundary of the computational domain is placed 100 chords away from the profile and the spanwise dimension is $0.2c$. Overlapping grid capabilities have been exploited to reduce the computational effort. The height of the first cell is always below 0.8 wall units in the laminar bubble and in the turbulent regions, whereas, streamwise and spanwise mesh sizes are less than 15 and 10 wall units, respectively.

Quantities of interest

The selected quantities of interest are the same as for the Eppler 387 airfoil: C_L and C_D coefficients along with the C_p and C_f coefficients on the airfoil surface. Experimental data are available for C_f, from Miozzi et al. [2020] with the "two-dimensional" results being determined based on the average of the experimental data in the spanwise direction and by fixing the experimental uncertainty equal to the standard deviation of the spanwise distributions of C_f.

Results

There are two main objectives for the present exercise:

1. Check the consistency of different RANS solvers with common mathematical models, grids, and boundary conditions;

2. Compare the results obtained with the k-ω SST model combined with the γ-Re_θ and γ transition models against the experimental data and also with the results from the LES simulations.

The first goal is addressed by evaluating the overlap between the intervals corresponding to the uncertainty bands associated with the computational predictions for the various quantities of interest. Such an exercise does not require the knowledge of experimental results and can be performed for all of the selected quantities of interest.

The comparison of RANS solutions with experimental data and the LES results is performed with the traditional graphical comparisons. Nonetheless, error bars are presented for both the numerical and experimental results, whenever available.

Table 4 presents the labels used in this section to identify the computational results obtained by using each flow solver. The table includes only the two-dimensional RANS computations that are compared during the solution verification exercises. We note that the designation IM corresponds to the ReFRESCO simulations with first-order upwind discretization of the convective terms of the k and ω transport equations, whereas IM2 correspond to the simulations with second-order upwind discretization for all transport equations.

All RANS computations were performed for an incompressible fluid ($M = 0$) with the exception of the calculations performed with FUN3D and OVERFLOW that are compressible flow solvers using $M = 0.1$ and low Mach precodintioning. Furthermore, as described above, several alternatives are used for the implementation of the production term of the k transport equation. Therefore, the RANS solvers are not using strictly the same mathematical model.

Table 4: Labels used to identify the simulations performed with the different RANS flow solvers used in the three test cases.

Institution	Flow Solver	Label
DRDC	ANSYS-CFX	DRDC
ECN-CNRS	ISIS-CFD	ECN
IST/MARIN	ReFRESCO	IM or IM2
NASA-LARC	FUN3D	LARC-F
NASA-LARC	OVERFLOW	LARC-O
SIREHNA	STAR-CCM+	SIRH

Table 5: RANS simulations performed for the T3AM and T3A settings of the flow over a flat plate.

	T3AM	
Institution	γ-Re_θ	γ
DRDC	HO 1-5	HO 1-5
ECN	O 1-5	O 1-5
IM	All grids	All grids
LARC-F	HO 4-9	
SIRH	HO 1,3,5,7,9	HO 1,3,5,7,9
	T3A	
Institution	γ-Re_θ	γ
DRDC	HO 1-5	HO 1-5
ECN	O 1-5	O 1-5
IM	HO 1-9	HO 1-9
LARC-F	HO 4-9	
SIRH	HO 1,3,5,7,9	HO 1,3,5,7,9

Iterative convergence

One of the challenges in applying the transition models during low Reynolds number RANS computations is to reduce the iterative error to negligible levels. The several RANS solvers used in this exercise used different strategies to handle the iterative errors.

The DRDC simulations (ANSYS-CFX) have an iterative convergence criteria that requires the L_∞ norm of the residuals for the continuity and momentum equations below 10^{-7} for the flat plate cases and below 10^{-8} for the airfoil cases.

In the ECN simulations (ISIS-CFD), there is no strict criterion for iterative convergence. Iterative convergence is monitored using the force coefficients and the distributions of pressure and skin friction coefficients at the plate and airfoil surfaces.

All IM and IM2 simulations (ReFRESCO) have the L_∞ norm of the normalized residuals of all transport equations solved reduced to values smaller than 10^{-8}. Normalized residuals are equivalent to nondimensional variable changes during a Jacobi iteration.

LARC-F (FUN3D) and LARC-O (OVERFLOW) simulations required a L_2 residual drop of at least 8 orders of magnitude for all transport equations.

The SIRH simulations (STAR-CCM+) require a drop of at least 4 orders of magnitude for the L_2 norm of the residual, but 8 orders of magnitude of residual drop was achieved for most simulations. Convergence of forces and moments is also checked.

Flow over a flat plate

The computations performed for the T3AM and T3A conditions of the flow over a flat plate are presented in Table 5. Figure 6 illustrates the results obtained with the different flow solvers for the C_f distributions and for the V_x and k profiles at $Re_x = 1.8281 \times 10^6$ for the T3AM settings. For the γ model the selected location is in the transition region in all the calculation, whereas for the γ-Re_θ model results and for the experiments it is at the end of the laminar region. The results correspond to the finest grids simulated with each solver and the estimated error bars are based on the data of five grids. The graphical agreement between the several results seems excellent, with the exception of the profiles obtained with the γ model that also exhibit the largest numerical uncertainties.

The consistency of the several RANS computations is checked by determining the overlap between the error bars obtained for all selected quantities of interest. The percentage of cases with nonoverlapping error bars and the largest discrepancies between two solutions are presented in Table 6. Most of the cases tested do not exhibit overlapping error bars for all simulations performed with the same mathematical model. The exception is the V_x profile in the transition region (x_2) of the T3AM simulations with the γ model where the estimated error bars are so large that there is overlap between all simulations. Nevertheless, there are two main trends in the data: the agreement between the different flow solvers tends to be better for the γ model than for the γ-Re_θ model; discrepancies for the mean flow quantity (V_x) tend to be smaller than those obtained for the turbulence and transition quantities.

Figure 7 presents the convergence with grid refinement of one location from each of the C_f, V_x and k results plotted in Figure 6. The plots of Figure 7 also include the least-squares fits used to estimate the numerical uncertainty. It is clear that grid convergence properties are strongly dependent on the flow solver. As expected, it is not easy to estimate the observed order of grid convergence due to scatter in the data and/or nonmonotonic con-

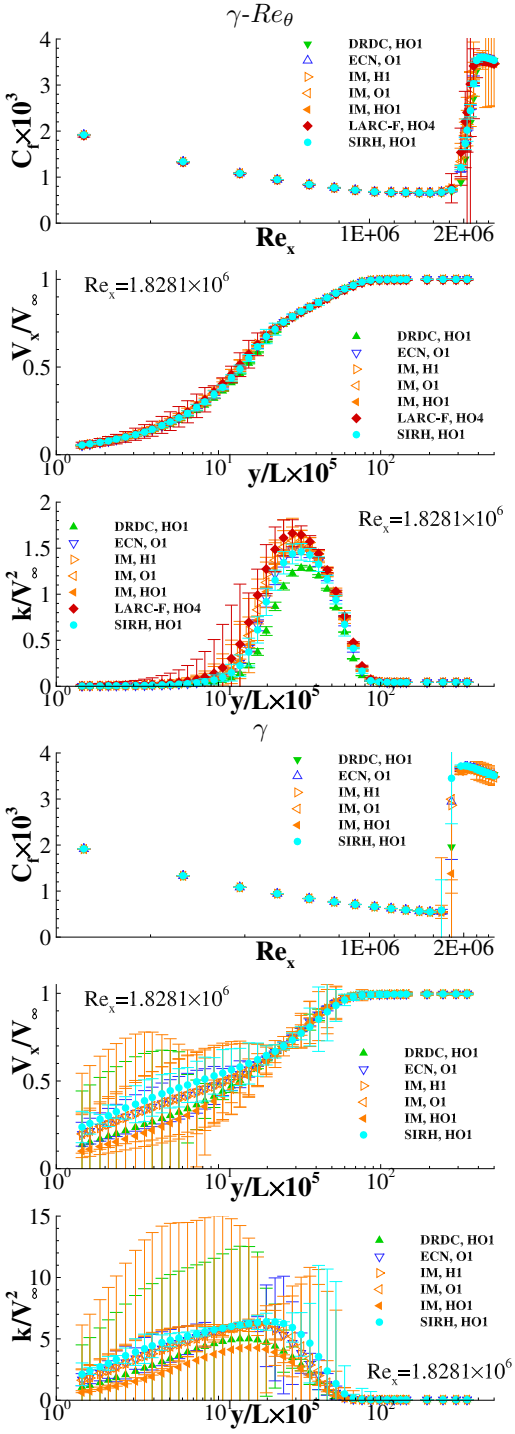

Figure 6: Comparison of the solutions obtained with different RANS solvers for the skin friction coefficient C_f and mean horizontal velocity component V_x and turbulence kinetic energy k profiles in the transition region. Flow over a flat plate for the T3AM conditions.

vergence. For the γ-Re_θ model, the DRDC results are not consistent with most of the other submissions, whereas for the γ model it is the SIRH results that are different from the other solutions.

Table 6: Percentage of locations for all quantities of interest where the error bars of the numerical solutions do not overlap and the largest discrepancy between any two numerical solutions for each case. Flow over a flat plate for the T3AM and T3A settings.

Percentage of cases with nonoverlapping error bars

		T3AM		T3A	
Variable		γ-Re_θ	γ	γ-Re_θ	γ
$C_f \times 10^3$		100.	92.3	92.3	92.3
V_x/V_∞	x_1	100.	97.4	100.	82.4
	x_2	100.	0.	81.1	75.7
	x_3	95.6	67.4	100.	61.0
k/V_∞^2	x_1	92.3	94.9	88.2	79.4
	x_2	90.7	20.9	81.1	86.5
	x_3	93.5	56.4	70.7	82.9
ν_t/ν	x_1	97.4	69.2	76.5	64.7
	x_2	97.7	27.9	75.7	86.5
	x_3	97.8	65.2	56.1	70.7
γ	x_1	76.9	46.2	82.4	61.8
	x_2	95.3	48.8	86.5	97.3
	x_3	95.7	43.5	48.8	78.0

Largest discrepancy between two numerical solutions

		T3AM		T3A	
Variable		γ-Re_θ	γ	γ-Re_θ	γ
$C_f \times 10^3$		0.332	0.069	0.147	0.069
V_x/V_∞	x_1	0.008	0.003	0.016	0.013
	x_2	0.036	0.	0.015	0.018
	x_3	0.060	0.012	0.020	0.017
k/V_∞^2	x_1	0.076	0.003	0.035	0.031
$\times$	x_2	0.434	2.03	0.387	0.190
10^3	x_3	0.867	0.168	0.220	0.200
ν_t/ν	x_1	0.188	0.023	0.730	0.410
	x_2	2.03	1.70	0.548	0.408
	x_3	1.99	3.59	3.48	3.25
γ	x_1	0.012	0.066	0.033	0.071
	x_2	0.272	0.031	0.059	0.026
	x_3	0.262	0.056	0.023	0.054

Figure 8 compares the available experimental data (Roach and Brierley [1990]) with the RANS results using the SST k-ω turbulence model combined with the γ-Re_θ and γ transition models. The numerical results are obtained with ReFRESCO (IM) in the finest grid of the HO topology (HO1). The overall agreement between experiments and computations is better for the bypass transition case (T3A) than for natural transition (T3AM). Furthermore, the differences between the two transition models are larger for the T3AM results than for the T3A data. In the T3AM case, the very narrow transition region obtained with the γ model leads to a significant increase of

the estimated numerical uncertainties inside the transition region.

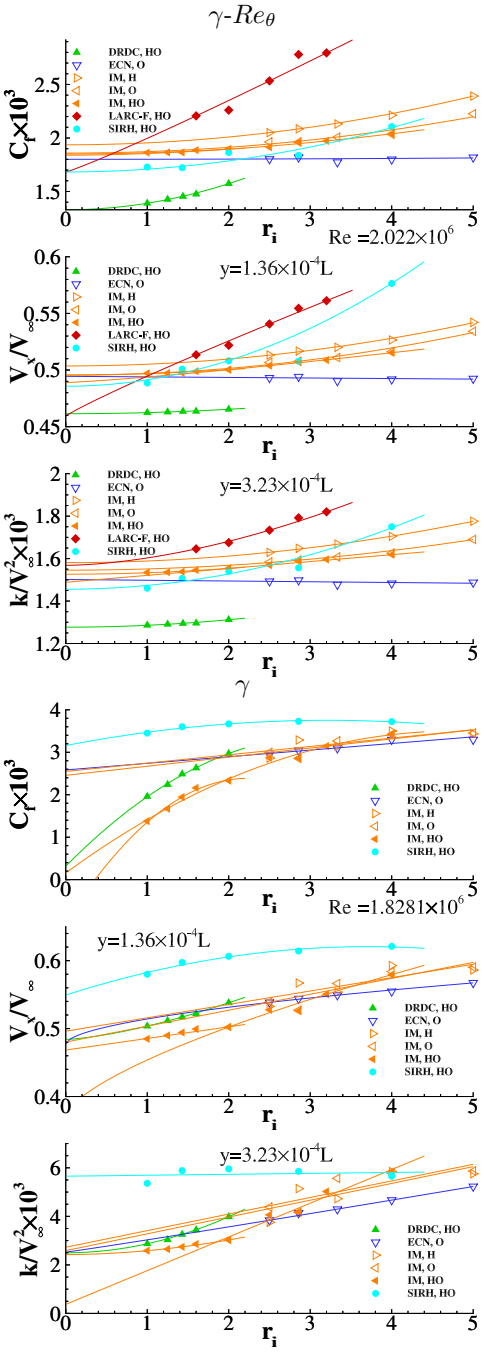

Figure 7: Illustration of the grid convergence of the skin friction coefficient C_f, mean horizontal velocity component V_x, and turbulence kinetic energy k obtained with different RANS solvers. Flow over a flat plate for the T3AM conditions.

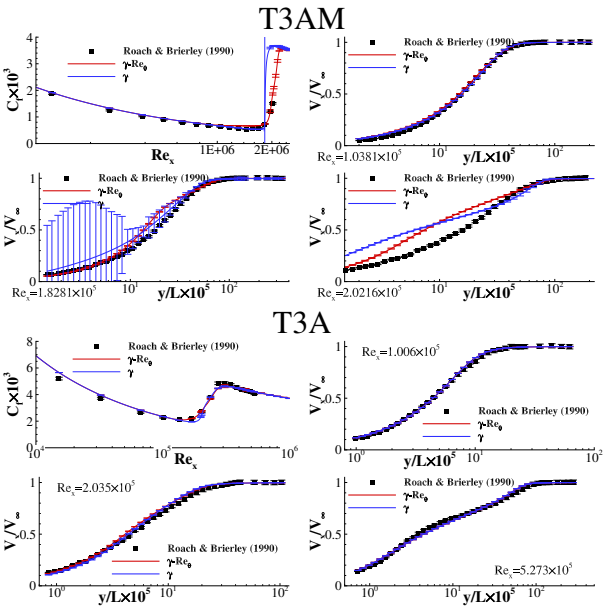

Figure 8: Comparison of the RANS solutions using the SST k-ω turbulence model combined with the γ-Re_θ and γ transition models with the experimental data (Roach and Brierley [1990]). Flow over a flat plate for the T3AM and T3A conditions.

Flow around the Eppler 387 airfoil

Table 7 presents the results available for the flow around the Eppler 387 airfoil at $\alpha = 1°$ and $\alpha = 7°$ with $Re = 3 \times 10^5$. Figure 9 presents the pressure coefficient C_p distributions on the airfoil surface and the skin friction coefficient C_f on the upper surface of the airfoil obtained with the several RANS solvers. The plot contains the solutions on the finest grid calculated by each solver and the error bars are based on the data obtained with 5 grids.

With the exception of the C_f distribution in the leading edge region, the graphical agreement between all the error bars seems excellent. However, as for the flat plate test cases, the check on the consistency between all of the RANS solutions in terms of an overlap between the error bars shows a different scenario. Table 8 presents the percentage of chordwise stations that do not exhibit overlapping error bars. Additionally, the table highlights the largest discrepancies between any two RANS solutions for coefficients C_{Df}, C_{Dp}, C_D and C_L, and for the C_p and C_f values at 56 locations on the upper and lower surfaces of the airfoil (28 on each side).

The results show that it is, in fact, rare to find overlapping error bars for the predictions based on the RANS solvers under consideration, even for the force coefficients. Only the γ model for $\alpha = 7°$ exhibits 3 consistent force coefficients (C_{Dp}, C_D, and C_L). Nonetheless, there

Table 7: RANS simulations performed for the flow around the Eppler 387 airfoil at $\alpha = 1^\circ$ and $\alpha = 7^\circ$ with $Re = 3 \times 10^5$.

	$\alpha = 1^\circ$	
Institution	γ-Re_θ	γ
DRDC	CO 5-9	CO 5-9
ECN	CO 1-5	CO 1-5
IM	All grids	All grids
IM2	CO 1-5	CO 1-5
LARC-F	CO 5-9	
LARC-O	CO 5-9	
SIRH	CO 1,3,5,7,9	HO 1,3,5,7,9
	$\alpha = 7^\circ$	
Institution	γ-Re_θ	γ
DRDC	CO 5-9	CO 5-9
IM	All grids	All grids
IM2	CO 1-5	CO 1-5
LARC-F	CO 5-9	
LARC-O	CO 5-9	
SIRH	CO 1,3,5,7,9	HO 1,3,5,7,9

Table 8: Percentage of locations for all quantities of interest where the error bars of the numerical solutions do not overlap and largest discrepancy between two numerical solutions for each case. C_ϕ corresponds to $C_{Df} \times 10^3$, $C_{Dp} \times 10^3$, $C_D \times 10^3$ and C_L. Flow around the Eppler 387 airfoil at $\alpha = 1^\circ$ and $\alpha = 7^\circ$ with $Re = 3 \times 10^5$.

Percentage of cases with non overlapping error bars

		$\alpha = 1^\circ$		$\alpha = 7^\circ$	
Variable		γ-Re_θ	γ	γ-Re_θ	γ
C_ϕ		100.	75.	100.	25.
C_p	Upper	100.	100.	100.	89.3
	Lower	100.	100.	100.	96.4
C_f	Upper	96.4	92.9	100.	78.6
$\times 10^3$	Lower	78.6	75.0	64.3	21.4

Largest discrepancy between two numerical solutions

		$\alpha = 1^\circ$		$\alpha = 7^\circ$	
Variable		γ-Re_θ	γ	γ-Re_θ	γ
C_ϕ		1.13	0.029	4.56	0.018
C_p	Upper	0.106	0.020	0.236	0.020
	Lower	0.025	0.008	0.094	0.018
C_f	Upper	4.60	4.30	5.21	2.17
$\times 10^3$	Lower	0.616	0.940	7.11	0.210

are two trends that can be observed in the data of Table 8: consistency of the several RANS solutions is better for the γ model than for the γ-Re_θ model; there is better agreement between the different RANS solutions for C_f than for C_p.

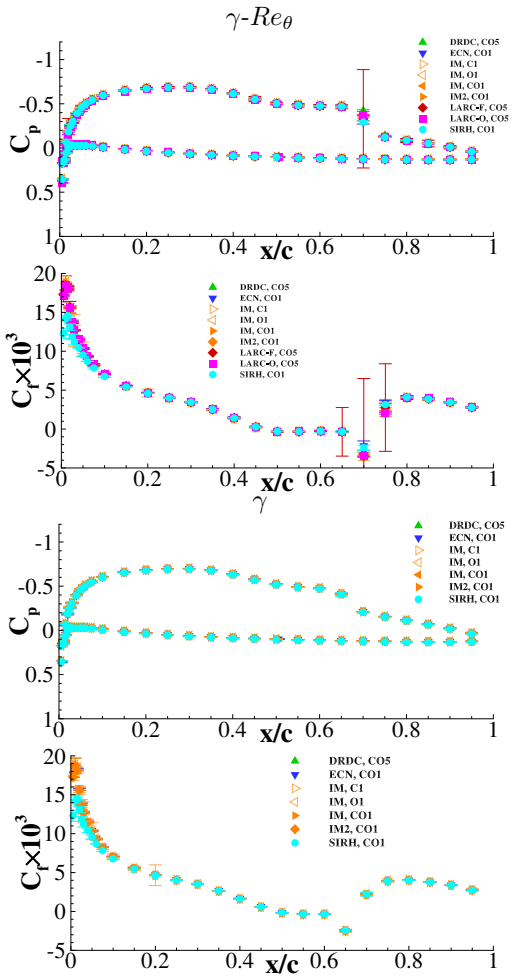

Figure 9: Comparison of the solutions obtained with different RANS solvers for the pressure coefficient C_p on the airfoil surface and for the skin friction C_f coefficient on the upper surface of the airfoil. Flow around the Eppler 387 airfoil at $\alpha = 1^\circ$ and $Re = 3 \times 10^5$.

Convergence of the quantities of interest with grid refinement for the different RANS solvers is illustrated in Figure 10 for the drag coefficient C_D and for one location in the laminar separation bubble on the upper surface of the airfoil at $\alpha = 1^\circ$. The results show significant differences between the grid convergence properties of the different RANS solvers. There is a clear reduction of the grid dependency of ReFRESCO with the use of second-order upwind discretization for the convective terms in the k and ω transport equations (IM2, CO) when compared to the first-order approach (IM, CO). Some of the large uncertainties estimated for the laminar separation region are a consequence of scatter in the data, as for example the C_p and C_f of the LARC-F results with the γ-Re_θ model.

When there is scatter in the data, nonmonotonic convergence can be the best fit to the data and that can lead

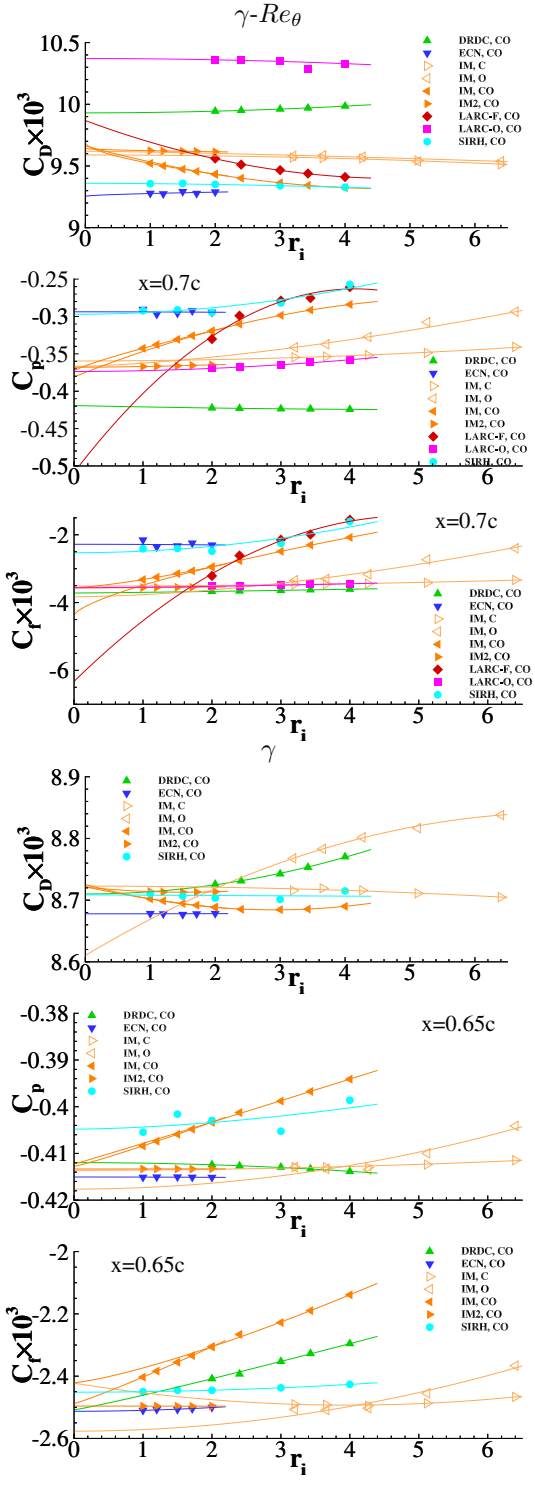

Figure 10: Illustration of the grid convergence of the drag coefficient C_D, pressure coefficient C_p and skin friction coefficient C_f in the laminar separation bubble of the upper surface obtained with different RANS solvers. Flow around the Eppler 387 airfoil at $\alpha = 1°$ and $Re = 3 \times 10^5$.

to large uncertainty bars. The locations of Figure 10 were selected to illustrate this difficulty. The origin of the scatter can be max/min functions in the turbulence and transition models, limiters in the discretzation schemes and/or insufficient iterative convergence.

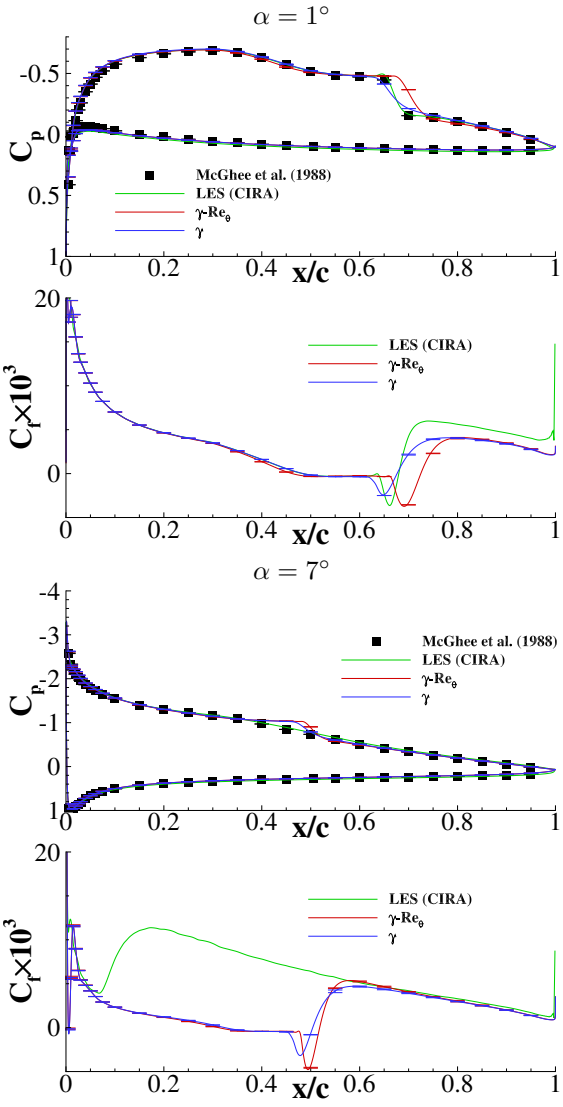

Figure 11: Comparison of the RANS solutions using the SST k-ω turbulence model combined with the γ-Re_θ and γ transition models with the experimental data (McGhee et al. [1988]). Flow around the Eppler 387 airfoil at $\alpha = 1°$ and $\alpha = 7°$ with $Re = 3 \times 10^5$.

The IM2 C_p distributions on the airfoil surface obtained on the finest grid with the γ-Re_θ and γ transition models are compared with the experimental data from McGhee et al. [1988] in Figure 11. The plots also contain the C_p and C_f distributions of the LES simulations reported in Catalano and de Rosa [2020] that are designated in the figure as LES (CIRA). The numerical uncer-

tainty in the RANS computations is also plotted in the figures, but its magnitude is rather small being comparable to the line thickness. For $\alpha = 1°$, the largest discrepancies relative to the experimental data are obtained for the γ-Re_θ model that leads to the largest laminar separation bubble. The experiments and the LES results do not exhibit a laminar separation bubble for $\alpha = 7°$, whereas the RANS results exhibit a laminar separation bubble for the two transition models. Transition location is significantly upstream in the case of LES simulations, but it occurs almost near midchord, after laminar separation, in the case of RANS-based transition model results. We recall that the inlet values of k and ω used in the RANS simulations lead to a very low turbulence intensity at the leading edge, $I \simeq 6 \times 10^{-3}$.

Flow around the NACA 0015 airfoil

There is only one set of CO grids proposed for the simulation of the flow around the NACA 0015 airfoil at $\alpha = 5°$ and $\alpha = 10°$ with $Re = 1.8 \times 10^5$. Table 9 presents the RANS solutions performed for this test case.

Table 9: RANS computations performed for the flow around the NACA 0015 airfoil at $\alpha = 5°$ and $\alpha = 10°$ with $Re = 1.8 \times 10^5$.

$\alpha = 5°$		
Institution	γ-Re_θ	γ
DRDC	CO 5-9	CO 5-9
ECN	CO 5-9	CO 5-9
IM	CO 1-9	CO 1-9
LARC-F	CO 5-9	
LARC-O	CO 5-9	
$\alpha = 10°$		
Institution	γ-Re_θ	γ
DRDC	CO 5-9	CO 5-9
IM	CO 1-9	CO 1-9

The pressure coefficient C_p on the airfoil surface and the skin friction coefficient C_f on the upper surface obtained with the several RANS solvers are presented in Figure 12 for $\alpha = 5°$ and $Re = 1.8 \times 10^5$. Discrepancies involving the laminar separation region between the different RANS solutions with the γ-Re_θ model are much larger than those observed for the Eppler 387 airfoil. On the other hand, the 3 solutions calculated with the γ model are in excellent graphical agreement.

The check for the consistency in terms of an overlap between the errors bars obtained for all the quantities of interest with the different RANS solvers shows again that the majority of the quantities of interest do not exhibit

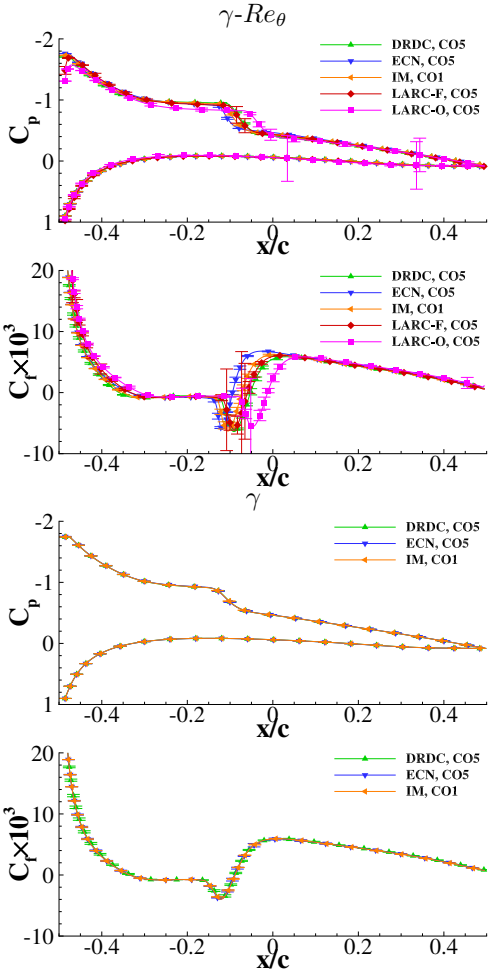

Figure 12: Comparison of the solutions obtained with different RANS solvers for the pressure coefficient C_p on the airfoil surface and for the skin friction C_f coefficient on the upper surface of the airfoil. Flow around the NACA 0015 airfoil at $\alpha = 5°$ and $Re = 1.8 \times 10^5$.

overlapping error bars. As illustrated by the plots of Figure 12 and Table 10, the largest discrepancies between any two solutions are significantly larger for the γ-Re_θ model than for the γ model. Although there is still a large percentage of nonoverlapping error bars for the γ solutions, the largest discrepancies between any two numerical solutions are very small, especially for $\alpha = 5°$.

The convergence of the drag coefficient C_D , and C_p and C_f values at a location in the laminar separation bubble with grid refinement is illustrated in Figure 13 for the flow at $\alpha = 5°$. It is clear that the discrepancies obtained for the γ-Re_θ model are not justified by the numerical uncertainty. Nonetheless, the data do show some cases with noisy convergence and others with nonmonotonic convergence, making the estimation of numerical uncertainty challenging.

Table 10: Percentage of locations for all quantities of interest where the error bars of the numerical solutions do not overlap and largest discrepancy between two numerical solutions for each case. C_ϕ corresponds to $C_{Df} \times 10^3$, $C_{Dp} \times 10^3$, $C_D \times 10^3$ and C_L. Flow around the NACA 0015 airfoil at $\alpha = 5°$ and $\alpha = 10°$ with $Re = 1.8 \times 10^5$.

Percentage of cases with non overlapping error bars

		$\alpha = 5°$		$\alpha = 10°$	
Variable		γ-Re_θ	γ	γ-Re_θ	γ
C_ϕ		100.	25.	100.	50.
C_p	Upper	100.	58.7	96.9	69.3
	Lower	100.	100.	98.4	95.3
C_f	Upper	99.8	38.4	80.7	81.5
$\times 10^3$	Lower	90.9	51.9	42.1	61.0

Largest discrepancy between two numerical solutions

		$\alpha = 5°$		$\alpha = 10°$	
Variable		γ-Re_θ	γ	γ-Re_θ	γ
C_ϕ		7.08	0.001	3.17	0.127
C_p	Upper	0.447	0.001	0.265	0.005
	Lower	0.048	0.004	0.013	0.002
C_f	Upper	11.5	0.099	9.39	0.197
$\times 10^3$	Lower	2.07	0.015	0.208	0.013

The IM RANS solutions obtained on the finest grid are compared in Figure 14 with the experimental data reported in Miozzi et al. [2019]. There are data obtained with LES (LES, CIRA) reported in Catalano and de Rosa [2020] for the two angles of attack, in addition to another LES performed with Xnavis (LES, CNR-INM) for $\alpha = 5°$. The LES results exhibit larger C_f values than the RANS solution in the fully-turbulent region and also indicate better agreement with the experimental data. However, there are significant differences across the entire set of computational predictions within the laminar separation bubble, including the two LES results at $\alpha = 5°$. It should be stated that identifying the sign of wall shear-stress measured in the experiments is not straightforward. Therefore, the comparison of the separation and re-attachment points between the experiments and the computations is not reliable.

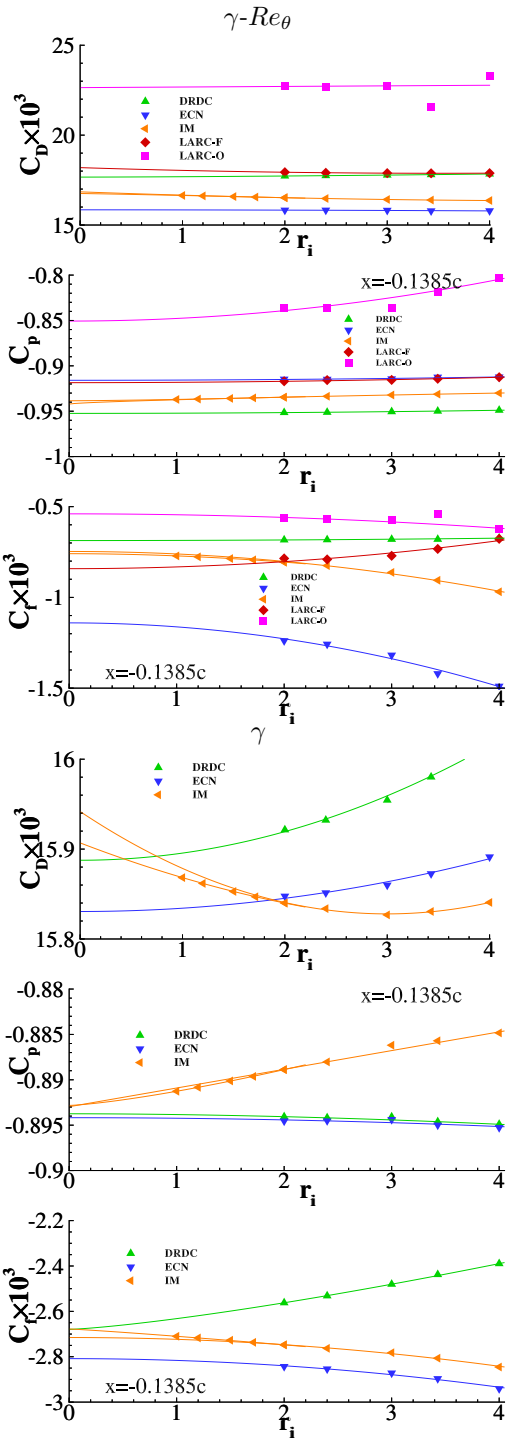

Figure 13: Illustration of the grid convergence of the drag coefficient C_D, pressure coefficient C_p and skin friction coefficient C_f in the laminar separation bubble of the upper surface obtained with different RANS solvers. Flow around the NACA 0015 airfoil at $\alpha = 5°$ and $Re = 1.8 \times 10^5$.

Conclusions

This paper presents the main results obtained during the first phase of the AVT-313 Workshops that was dedicated to the simulation of nominally 2D low Reynolds number flows with the RANS equations using the k-ω SST turbulence model and the $\gamma - Re_\theta$ and γ transition models. Three two-dimensional geometries (flat plate, Eppler 387 airfoil and NACA 0015 airfoil) are considered

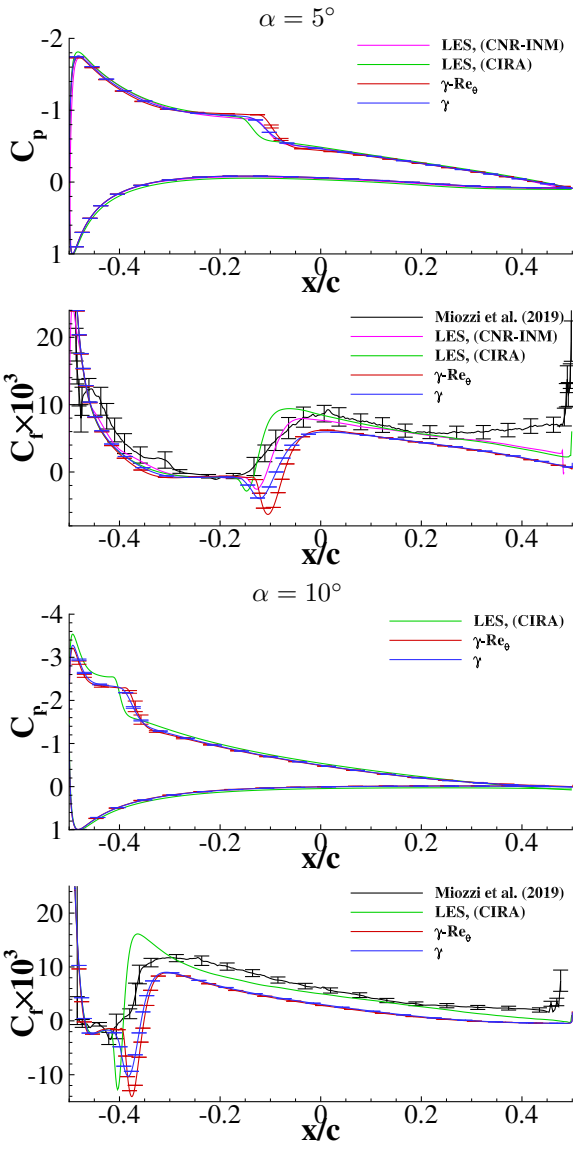

Figure 14: Comparison of the RANS solutions using the SST k-ω turbulence model combined with the γ-Re_θ and γ transition models with the experimental data Miozzi et al. [2019]. Flow around the NACA 0015 airfoil at $\alpha = 5°$ and $\alpha = 10°$ with $Re = 1.8 \times 10^5$.

to simulate steady flows of incompressible fluids.

The flat plate flow settings include one case of natural transition and one of bypass transition due to high freestream turbulence intensity. Two angles of attack were selected for each of the airfoils, yielding a total of four airfoil cases. Three of those flow settings lead to laminar separation bubbles on the upper surface of the airfoil (Eppler 387 at $\alpha = 1°$ and $Re = 3 \times 10^5$ and NACA 0015 at $\alpha = 5°$ and $\alpha = 10°$ and $Re = 1.8 \times 10^5$), whereas the occurrence of a laminar separation bubble for the Eppler 387 at $\alpha = 7°$ and $Re = 3 \times 10^7$ depends on the turbulence intensity of the incoming flow, which in the RANS computations is set to a low level.

Experimental data are available in the open literature for all of the selected test cases. However, all of the information required to simulate the flows at the exact conditions of the experiments is not available. Therefore, it is not possible to make a rigorous assessment of the modeling error in the selected mathematical models. Nonetheless, the available experimental data are compared with the results from the RANS computations and the LES, when available, for the airfoils test cases.

The main focus of the present exercise is the assessment of the consistency across the solutions obtained with different RANS solvers by using the same mathematical model, domain size and boundary conditions. To this end, geometrically similar grids have been generated for all of the test cases, including more than one grid topology for four out of the six test cases. Selected quantities of interest included integral quantities as well as local flow quantities on the surface and in the interior of the domain. For each test case, solutions are obtained for at least five grids from a given set, making it possible to estimate numerical uncertainties for all computed quantities of interest. Therefore, the influence of the different numerical techniques used in each RANS solver, grid density, and/or grid topology on the numerical solutions is taken into account in the estimated error bars.

It is important to recall that there are small differences in the details of the implementation of the turbulence and transition models in the different flow solvers. For example, it was identified that several alternatives are used for the implementation of the production term of the k transport equation. Therefore, it is not guaranteed that all RANS solvers are using strictly the same mathematical model.

The solution verification exercises lead to the following conclusions:

- Most of the consistency checks performed for all of the test cases showed nonoverlapping error bars for the solutions obtained with the nominally same mathematical model but different RANS solvers. In general, the discrepancies between the different numerical solutions are larger for the γ-Re_θ model than for the γ model. These results can be a consequence of the details of the implementation of the turbulence and transition models that are not strictly identical in all the flow solvers tested. Therefore, code to code comparisons is not a trivial exercise.

- The grid convergence properties obtained for the several quantities of interest are strongly dependent on the RANS solver. Furthermore, for a fixed RANS solver, the grid convergence properties depend on the selected flow quantity and/or the grid topology.

Therefore, single grid comparisons between different flow solvers can lead to misleading conclusions.

- In the transition region, the numerical uncertainties obtained for the γ model tend to be significantly larger than those obtained for the $\gamma - Re_\theta$ model. This is in large part a consequence of the steeper increase in C_f obtained for the γ model.

The comparisons of the RANS solutions with the data from experiments and the LES suggest the following remarks:

- For the flat plate cases, the differences between the $\gamma - Re_\theta$ and γ model solutions are larger for natural transition than for the bypass transition. There is also a much better agreement between experiments and the RANS computations for the bypass transition than for the natural transition conditions.

- For the Eppler 387 at $\alpha = 1°$, the best agreement between the RANS C_p distributions and the experiments is obtained with the γ model. The same trend is observed in the comparison between the RANS and LES results that also include C_f. At $\alpha = 7°$, the experiments and the LES results do not show a laminar separation bubble, whereas the RANS solutions exhibit a bubble at the midchord location. This result is likely to be a consequence of the extremely low turbulence intensity at the leading edge of the airfoil in the RANS simulations.

- The largest discrepancies between the results from the RANS simulations are observed for the flow around the NACA 0015 airfoil. The differences with respect to the experimental data are smallest in the fully turbulent region for the LES results, but the laminar separation bubbles are significantly different in both LES and RANS-based predictions, including the two LES results at $\alpha = 5°$.

The discrepancies exhibited by the different RANS computations and their respective error bars can have three causes: the estimated error bars are not conservative; the details of the nominal identical turbulence and transition models are not identical in all flow solvers; the implementations of the turbulence and transition models have "bugs". It is difficult to check the estimated error bars for the number of quantities of interest addressed in this study. Nonetheless, main problems should occur for coarse grids data leading to apparent second-order grid convergence. Although that was not thoroughly checked, it seems to be a rare situation. As mentioned above, there are differences in the details of the implementations of the turbulence and transition models and in the flow settings ($M = 0$ versus $M = 0.1$) that are contributing to the differences between flow solvers. Last but not the least, checking the existence of "bugs" can only be addressed with code verification. However, for the selected transition and turbulence models that is not a trivial exercise.

Currently, two-dimensional, steady RANS computations should be numerically accurate and enable the quantification of the modeling error. The lack of a test case with all the information required to simulate a low Reynolds number flow in identical conditions to the experiment hampers the ability to quantify accurately the modeling error of the simulations. However, it is not only the lack of complete information from experiments that makes it difficult. The same "nominal" turbulence and transition model may lead to different results due to different options in the details of the implementation. Nonetheless, it is clear that transition models are required for RANS based computations of low Reynolds number flows.

Acknowledgment

The authors would like to thank CIRA for their contributions to this exercise.

References

W. K. Anderson and D. L. Bonhaus. An Implicit Upwind Algorithm for Computing Turbulent Flows on Unstructured Grids. *Computers & Fluids*, 23(1):1–21, 1994.

ASME. *Standard for Verification and Validation in Computational Fluid Dynamics and Heat Transfer*. American Society of Mechanical Engineers, 2009.

AVT-313. `http://web.tecnico.ulisboa.pt/ist12278/Workshop_AVT_313_2D_cases/Workshop_AVT_313_2D_cases.htm`, 2022.

J. Baltazar, D. Rijpkema, and J. A. C. Falcão de Campos. On the Use of the γ-Re_θ Transition Model for the Prediction of the Propeller Performance at Model-Scale. *Ocean Engineering*, 170:6–19, 2018.

R. T. Biedron and J.R. Carlson et al. FUN3D Manual: 13.7. Technical report, NASA/TM-20205010139, 2020.

R. Broglia and D. Durante. Accurate prediction of complex free surface flow around a high speed craft using a single-phase level set method. *Computational Mechanics*, 62:421–437, 2018. doi: 10.1007/s00466-017-1505-1.

P. Catalano and D. de Rosa. Large Eddy Simulations and RANS Models for Airfoils at Low Reynolds Number.

In *AIAA AVIATION 2020 FORUM*, volume AIAA Paper 2020-2990, 2020.

P. Catalano, M. Wang, G. Iaccarino, and P. Moin. Numerical Simulation of the Flow Around a Circular Cylinder at High Reynolds Numbers. *International Journal of Heat and Fluid Flow*, 24(4):463–469, 2003.

G. M. Cole and T. J. Mueller. Experimental Measurements of the Laminar Separation Bubble on an Eppler 387 Airfoil at Low Reynolds Numbers. Technical report, NASA CR-186263, 1990.

A. Di Mascio, R. Broglia, and R. Muscari. On the Application of the One–Phase Level Set Method for Naval Hydrodynamic Flows. *Computers & Fluids*, 36(5): 868–886, 2007.

A. Di Mascio, R. Broglia, and R. Muscari. Prediction of hydrodynamic coefficients of ship hulls by high-order Godunov-type methods. *Journal of Marine Science and Technology*, 14(1):19–29, 2009. doi: 10.1007/s00773-008-0021-6.

L. Eça, R. Lopes, G. Vaz, J. Baltazar, and D. Rijpkema. Validation Exercises of Mathematical Models for the Prediction of Transitional Flows. In *Proceedings of the 31st Symposium on Naval Hydrodynamics*, 2016.

L. Eça and M. Hoekstra. The Numerical Friction Line. *Journal of Marine Science and Technology*, 13(4):328–345, 2008. doi: 10.1007/s00773-008-0018-1.

L. Eça and M. Hoekstra. A Procedure for the Estimation of the Numerical Uncertainty of CFD Calculations based on Grid Refinement Studies. *Journal of Computational Physics*, 262:104–130, 2014.

L. Eça, M. Hoekstra, and J. Windt. Practical Grid Generation Tools with Applications to Ship Hydrodynamics. In 8^{th} *International Conference on Numerical Grid Generation in Computational Field Simulations, Honolulu, Hawaii, U.S.A.*, 2002.

L. Eça, C.M. Klaij, G. Vaz, M. Hoekstra, and F.S. Pereira. On Code Verification of RANS Solvers. *Journal of Computational Physics*, 310:418–439, 2016. ISSN 0021-9991.

N. Franck and F. Ducros. Subgrid-Scale Stress Modelling Based on the Square of the Velocity Gradient Tensor. *Flow Turbulence and Combustion*, 62:183–200, 09 1999.

M. Kato and B. E. Launder. The modeling of Turbulent Flow Around Stationary and Vibrating Square Cylinders. In *9th Symposium on Turbulent Shear Flows*, 1993.

P. Khayatzadeh and S. Nadarajah. Laminar-Turbulent Flow Simulation for Wind Turbine Profiles Using the γ-Re_θ Transition Model. *Wind Energy*, 17(6):901–918, 2014.

D. Kim, Y. Kim, J. Li, R. V. Wilson, J. E. Martin, and P. M. Carrica. Boundary Layer Transition Models for Naval Applications: Capabilities and Limitations. *Journal of Ship Research*, 63(04):294–307, 12 2019.

C. M. Klaij and C. Vuik. SIMPLE-Type Preconditioners for Cell-Centered, Collocated Finite Volume Discretization of Incompressible Reynolds-Averaged Navier-Stokes equations. *International Journal for Numerical Methods in Fluids*, 71(7):830–849, 2013.

R. B. Langtry and F. R. Menter. Correlation-Based Transition Modeling for Unstructured Parallelized Computational Fluid Dynamics Codes. *AIAA Journal*, 47(12): 2894–2906, 2009. doi: 10.2514/1.42362.

A. Leroyer and M. Visonneau. Numerical Methods for RANS simulations of a Self-Propelled Fish-like Body. *Journal of Fluids and Structures*, 20:975–991, 2005.

R. Lopes, L. Eça, and G. Vaz. On the Numerical Behavior of RANS-Based Transition Models. *Journal of Fluids Engineering*, 142(5), 02 2020. 051503.

R. Lopes, L. Eça, M. Kerkvliet, and S. L. Toxopeus. Predicting Transition for the 6:1 Prolate Spheroid Using the RANS Equations. In *AIAA SCITECH 2022 Forum*, volume AIAA 2022-2570, 2022.

R. J. McGhee, S. W. Betty, and B. F. Millard. Experimental results for the eppler 387 airfoil at low reynolds numbers in the langley low-turbulence pressure tunnel. Technical report, NASA Technical Memorandum 4062, 1988.

F. R. Menter, M. Kuntz, R. Langtry, Y. Nagano, M. J. Tummers, and K. Hanjalic. Ten Years of Industrial Experience with the SST Turbulence Model. In *4th Internal Symposium, Turbulence, Heat and Mass transfer*, volume 4, pages 625–632, New York, 2003. Begell House. ISBN 1567001963.

F. R. Menter, R. B. Langtry, S. R. Likki, Y. B. Suzen, P. G. Huang, and S. Volker. A Correlation-Based Transition Model Using Local Variables-Part I: Model Formulation. *Journal of Turbomachinery*, 128(3):413–422, 03 2004.

F. R. Menter, P. E. Smirnov, T. Liu, and R. Avancha. A One-Equation Local Correlation-Based Transition Model. *Flow, Turbulence and Combustion*, 95(4):583–619, 2015. doi: 10.1007/s10494-015-9622-4.

T. F. Miller and F. W. Schmidt. Use of a Pressure-Weighted Interpolation Method for the Solution of the Incompressible Navier-Stokes Equations on a Nonstaggered Grid System, journal = Numerical Heat Transfer. 14(2):213–233, 1988.

M. Miozzi, A. Capone, M. Costantini, L. Fratto, C. Klein, and F. Di Felice. Skin friction and coherent structures within a laminar separation bubble. *Experiments in Fluids*, 60, 2019.

M. Miozzi, F. Di Felice, C. Klein, and M. Costantini. Taylor Hypothesis Applied to Direct Measurement of Skin Friction Using Data from Temperature Sensitive Paint. *Experimental Thermal and Fluid Science*, 110, 2020.

R. H Nichols and P. G. Buning. Users Manual for OVERFLOW 2.3, Version 2.3. Technical report, NASA Langley Research Center, 2019.

R. H. Nichols, R. W. Tramel, and P. G. Buning. Solver and Turbulence Model Upgrades to OVERFLOW 2 for Unsteady and High-Speed Applications. In *24th AIAA Applied Aerodynamics Conference*, volume AIAA Paper 2006-2824, 2006.

E. J. Nielsen, J. Lu, M. A. Park, and D. L. Darmofal. An Implicit, Exact Dual Adjoint Solution Method for Turbulent Flows on Unstructured Grids. *Computers and Fluids*, 33(9):1131–1155, 2004.

P. Queutey and M. Visonneau. An Interface Capturing Method for Free-Surface Hydrodynamic Flows. *Computers & Fluids*, 36:1481–1510, 11 2007. doi: 10.1016/j.compfluid.2006.11.007.

M. J. Raw. Robustness of coupled algebraic multi-grid for the Navier-Stokes equation. In *34th AIAA Aerospace and Sciences Meeting and Exhibit*, volume AIAA Paper 96-0297, 1996.

P. E. Roach and D. H. Brierley. The Influence of a Turbulent Free Stream on Zero Pressure Gradient Transitional Boundary Layer Development. Part 1: Testcases T3A and T3B. In *In Numerical simulation of unsteady flows and transition to turbulence*, 1990.

P. Roe. Approximate Riemann Solvers, Parameter Vector, and Difference Schemes. *Journal of Computational Physics*, 43:357–372, 10 1981.

M. S. Selig. *Summary of Low Speed Airfoil Data*. Number vol. 1 in Summary of Low Speed Airfoil Data. SoarTech Publications, 1995.

C. Seyfert and A. Krumbein. Evaluation of a Correlation-Based Transition Model and Comparison with the eN Method. *Journal of Aircraft*, 49(6):1765–1773, 2012.

M. Vinokur. On One-Dimensional Stretching Functions for Finite-Difference Calculations. *Journal of Computational Physics*, 50(2):215–234, 1983.

J. Wackers, G. Deng, E. Guilmineau, A. Leroyer, P.k Queutey, and M. Visonneau. Combined Refinement Criteria for Anisotropic Grid Refinement in Free-Surface Flow Simulation. *Computers & Fluids*, 92, 01 2013.

M. Wang, P. Catalano, and G. Iaccarino. Prediction of High Reynolds Number Flow Over a Circular Cylinder Using LES with Wall Modeling. 01 2001.

D. C. Wilcox. *Turbulence Modeling for CFD*. 1st Edition, DCW Industries, Inc., 1998.